Welding Metallurgy of Dissimilar AISI 430/DQSK Steels Resistance Spot Welds

The metallurgical behavior of dissimilar resistance spot welds in AISI 430 ferritic stainless steel and DQSK low-carbon steels is investigated

BY M. POURANVARI, S. P. H. MARASHI, AND M. ALIZADEH-SH

ABSTRACT

This paper addresses the microstructure and mechanical performance of dissimilar resistance spot welds between AISI 430 ferritic stainless steel and drawing quality special killed (DQSK) low-carbon steel. The mechanical properties of the welds are described by peak load, failure energy, and failure mode during the tensile-shear test. Phase transformations in the fusion zone (FZ) and heat-affected zone (HAZ) are analyzed. The main metallurgical features of the weldment are the formation of a dual-phase, ferrite-martensite microstructure in the FZ, grain growth and martensite formation in the HAZ of the ferritic stainless steel side, and martensitic and eutectoid transformations in the HAZ of the DQSK steel side. It was observed that increasing welding current leads to transition of failure mode from interfacial to double pullout mode. It is shown that the FZ size at sheet/sheet interface in the DQSK side is the key macrostructural feature controlling the load bearing capacity and energy absorption capability of the AISI 430/DQSK dissimilar weld.

KEYWORDS

• Resistance Spot Welding • Dissimilar Welding • Failure Mode
• Ferritic Stainless Steel • Welding Metallurgy

Introduction

Resistance spot welding (RSW) is a critical joining process in vehicle production. Vehicle crashworthiness, which is defined as the capability of a car structure to provide adequate protection to its passengers against injuries in the event of a crash, largely depends on the integrity and mechanical performance of the spot welds. The failure mode of resistance spot welds is a qualitative measure of mechanical properties (Refs. 1–3). Basically, spot welds can fail in two distinct modes, described as follows (Refs. 4–9):

1) Interfacial failure (IF) mode in which the fracture propagates through the fusion zone (FZ). It is believed that this failure mode has a detrimental effect on the crashworthiness of the vehicles.

2) Pullout failure (PF) mode in which the failure occurs via withdrawal of the weld nugget from one sheet. In this mode, fracture may initiate in the base metal (BM), heat-affected zone (HAZ), or HAZ/FZ depending on the metallurgical and geometrical characteristics of the weld zone and loading conditions. Generally, the pullout mode is the preferred failure mode due to its associated higher plastic deformation and energy absorption.

Due to its significant impact on joint reliability, failure mode has been an interesting issue for some recent studies. The transition from IF to PF mode is generally related to the increase in the size of FZ above a minimum value. It has been shown that the minimum FZ size is a function of sheet thickness and BM/HAZ/FZ materials properties as well as loading conditions (Refs. 10–17). It is shown that the hardness characteristics are the key controlling factor in failure mode transition of resistance spot welds, which in turn is governed by phase transformation in the FZ and HAZ. The nonequilibrium heating and cooling condition of RSW processes changes the phase stability of the weldment. Therefore, studying the phase transformations in the FZ and HAZ is critical for understanding the failure mode behavior and mechanical properties of the joints.

An unavoidable practical requirement in modern vehicle construction technology is dissimilar welding. Understanding the failure mode and failure behavior of similar spot welds is straightforward. However, the failure behavior of dissimilar resistance spot welds can be problematic due to the following reasons (Refs. 16, 18–20):

1) The difference in the physical properties of the base metals.

2) The difference in the materials properties (strength, ductility, and work hardening) of the base metals.

3) The more complicated microstructural gradient across the weld.

4) The mixing of the steels in the FZ, which affects the phase transformation in the weld nugget.

M. POURANVARI (pouranvari@sharif.edu) *is with the Department of Materials Science and Engineering, Sharif University of Technology, Tehran, Iran. S. P. H. MARASHI and M. ALIZADEH-SH are with the Mining and Metallurgical Engineering Department, Amirkabir University of Technology, Tehran, Iran.*

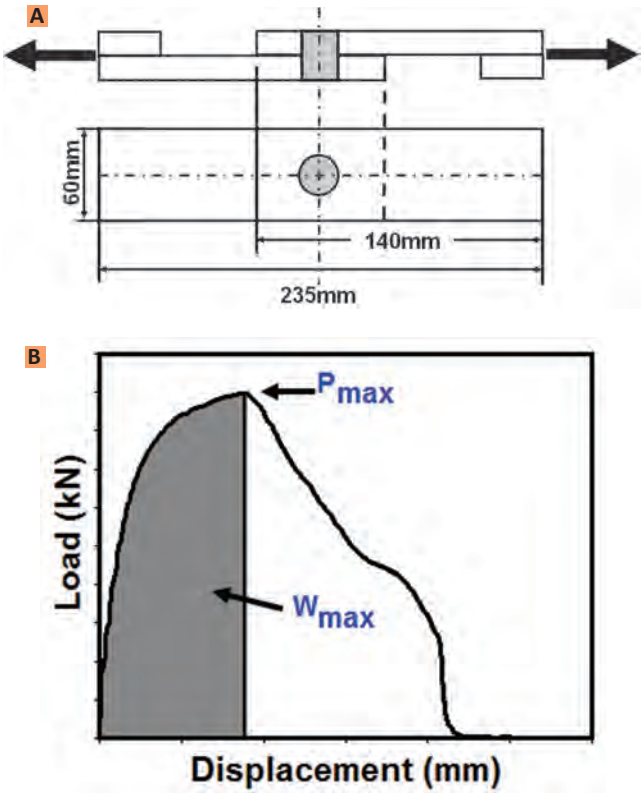

Fig. 1 — A — The tensile-shear specimen dimensions; B — a typical load-displacement curve along with the extracted parameters. P_{max}: Peak load, W_{max}: Energy absorption.

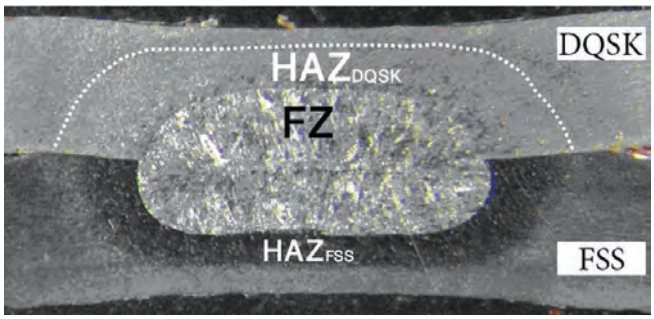

Fig. 2 — Typical macrostructure of dissimilar AISI 430 ferritic stainless steel (DQSK) and drawing quality special killed (DQSK) low-carbon steel.

Nowadays, ferritic stainless steels (FSSs) are widely used in structural frameworks and body paneling of buses and coaches. Since traditional steel grades are also widely used for automotive production, dissimilar RSW of both steels is an unavoidable practical requirement in modern vehicle design. Although physical attributes of spot welds, particularly FZ size, have significant influence on mechanical properties and failure mode behavior, phase transformations in weldment should also be considered to better understand the performance of the RSW joints.

Therefore, the present paper aims at investigating the welding metallurgy of dissimilar RSW of ferritic stainless steel and DQSK low-carbon steel. The phase transformations in the FZ and HAZs are detailed, and the effects of microstructural characteristics on failure mode and mechanical properties of the welds are discussed.

Experimental Procedure

AISI 430 ferritic stainless steels and DQSK AISI 1004 low-carbon steel were used as base metals in this research. The thickness of both sheets was 1.5 mm. The chemical compositions of the base metals were determined using a standard spark emission spectrometer (quantometer). Table 1 shows the chemical composition of the base metals.

Resistance spot welding was performed using a PLC-controlled, 120-kVA, AC pedestal-type RSW machine. Welding was conducted using a 45-deg truncated cone RWMA Class 2 electrode with an 8-mm face diameter. The welding process was performed with a constant electrode tip force of 3.3 kN. The welding current was increased from 6 to 11 kA with an increment of 0.5 kA. Throughout the process, squeeze, welding, and holding times were kept constant at 40, 12, and 20 cycles, respectively.

To evaluate the mechanical performance and failure mode of the spot welds, the tensile-shear test was performed. The tensile-shear test samples were prepared according to ANSI/AWS/SAE/D8.9-97 standard (Ref. 21).

Figure 1A shows the tensile-shear sample dimensions. The tensile-shear tests were performed at a cross head of 10 mm/min with a 20-ton Instron® universal testing machine. Failure modes were determined from the failed samples. Peak load (measured as the peak point in the load-displacement curve) and failure energy (measured as the area under the load-displacement curve up to the peak load) were extracted from the load displacement curve — Fig. 1B. The amount of failure energy was calculated by measuring the area under the load-displacement curve up to the peak load.

Microstructure characterization of the weldment was conducted by performing standard metallography procedure, and the specimens were etched by Kalling's No. 1 (33 mL H_2O, 1.5 g $CuCl_2$, 33 mL HCl, 33 mL ethanol) and 2% Nital (2 mL HNO_3, 98 mL ethanol). The FZ size was measured on the metallographic cross sections at the low-carbon steel side. A Vickers microhardness test was performed to obtain a diagonal hardness profile using an indenter load of 10 g.

Table 1 — Chemical Composition of Inves gated Steels (wt-%)

Steel	C	Mn	Si	Cr	Ni	Mo
AISI430 FSS	0.024	0.513	0.383	17.002	0.066	0.026
DQSK Low-Carbon Steel	0.044	0.202	0.001	0.010	0.031	0.003

Results and Discussion

Metallurgical Characteristics

Figure 2 illustrates a typical macrograph of the dissimilar FSS/DQSK resistance spot weld showing three distinct structural zones, including FZ or weld nugget, HAZ, and BM. Owing to the lower thermal conductivity and higher electrical resistivity of the FSS sheet compared to the DQSK sheet, the FZ has asymmetrical shape such that the volume fraction of weld metal in the FSS sheet is slightly larger than that of the DQSK sheet.

HAZ of AISI 430 Steel

Figure 3A shows the microstructure of the AISI 430 base metal indicating a fully ferritic microstructure along with carbides, which are evenly distributed throughout the matrix. In the HAZ, the base metal microstructure is influenced by phase transformations induced by the welding thermal cycle.

A pseudo-binary diagram of Fe-C-17Cr (Ref. 22) (Fig. 3B) is useful to describe the physical metallurgy and analyze the phase transformations in the HAZ of AISI 430 steel. Figure 3C shows the microstructure gradient in the HAZ of the FSS side. The phase transformations in the HAZ of AISI 430 steel welds have been discussed elsewhere (Ref. 23). According to the temperature distribution, the HAZ can be divided into two distinct metallurgical transformation zones, namely, high-temperature HAZ (HTHAZ) and low-temperature HAZ (LTHAZ).

The phase transformations in these zones are detailed as follows:

1) HTHAZ. Based on the pseudo-binary diagram (Fig. 3B), in this region, BM microstructure transforms to fully δ-ferrite microstructure at the elevated temperature. The carbide precipitates in the BM are completely dissolved. Upon cooling, a ferritic microstructure is retained and some reprecipitation of the carbides occurred — Fig. 3D.

The absence of a high-temperature austenite phase in the HTHAZ has two consequences:

- The austenite at the grain boundaries at elevated temperature can act to inhibit ferrite grain growth by pinning the grain boundaries. Therefore, ferrite grain growth at this region can be quite dramatic, as is evident from Fig. 3C. As can be seen, the grain growth is inversely proportional to the distance from the fusion line.
- Any austenite that may have formed at the elevated temperature will transform to martensite during the cooling cycle. Therefore, due to the absence of the high-temperature austenite, an almost martensite-free microstructure is formed in HTHAZ during cooling — Fig. 3C.

2) LTHAZ. Based on the pseudo-binary diagram (Fig. 3B), in this region, the BM microstructure transforms to δ-ferrite plus austenite at the elevated temperature. The amount of austenite at the grain boundaries of δ-ferrite strongly depends on the carbon con-

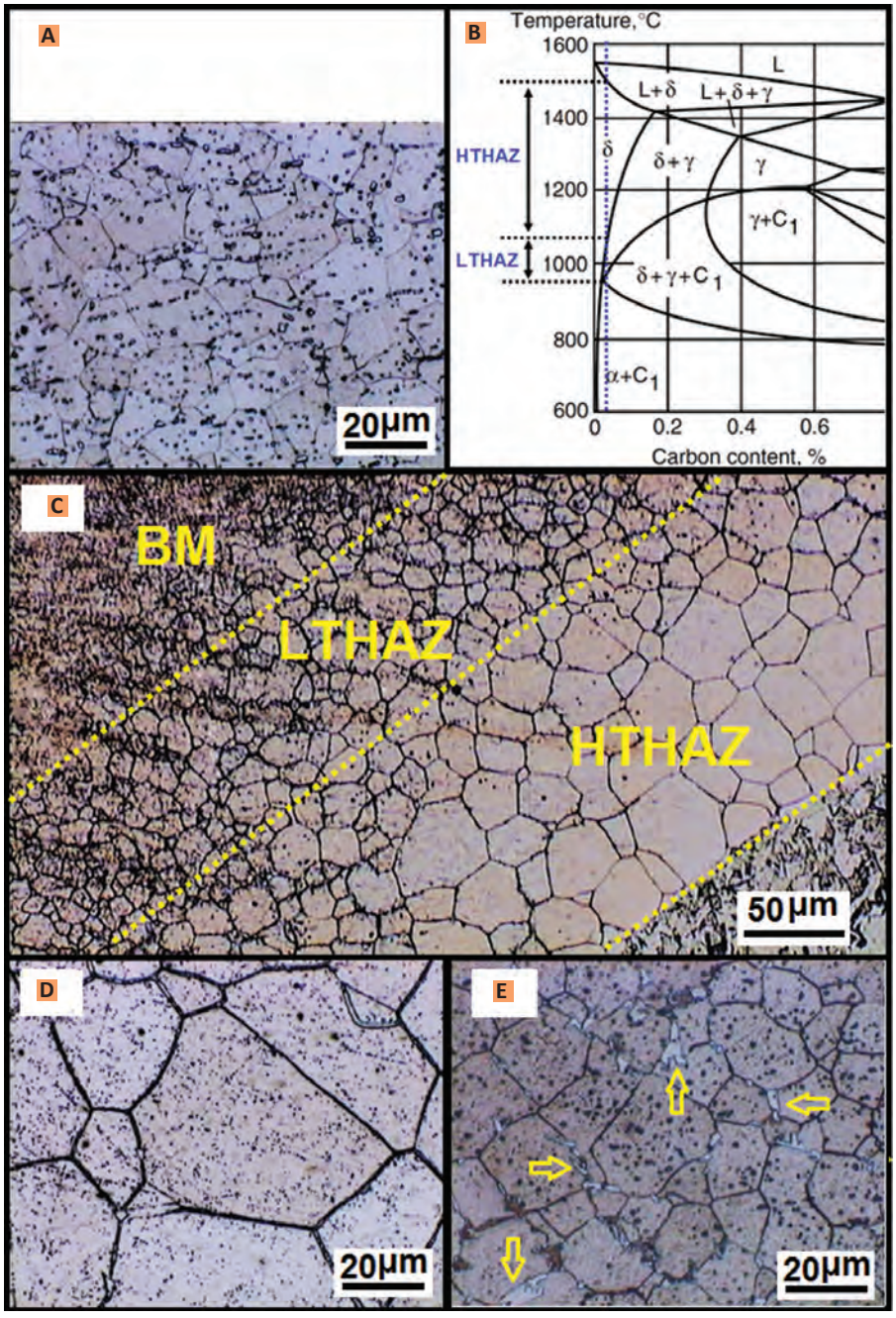

Fig. 3 — A — Base metal microstructure of AISI 430 steel; B — Fe-17% Cr-C phase diagram and HAZ of AISI 430 steel; C — microstructure gradient in the HAZ of ferritic stainless steel; D — grain growth and dispersion of carbide precipitates in HTHAZ; E — martensite formation, indicated by arrows, in LTHAZ.

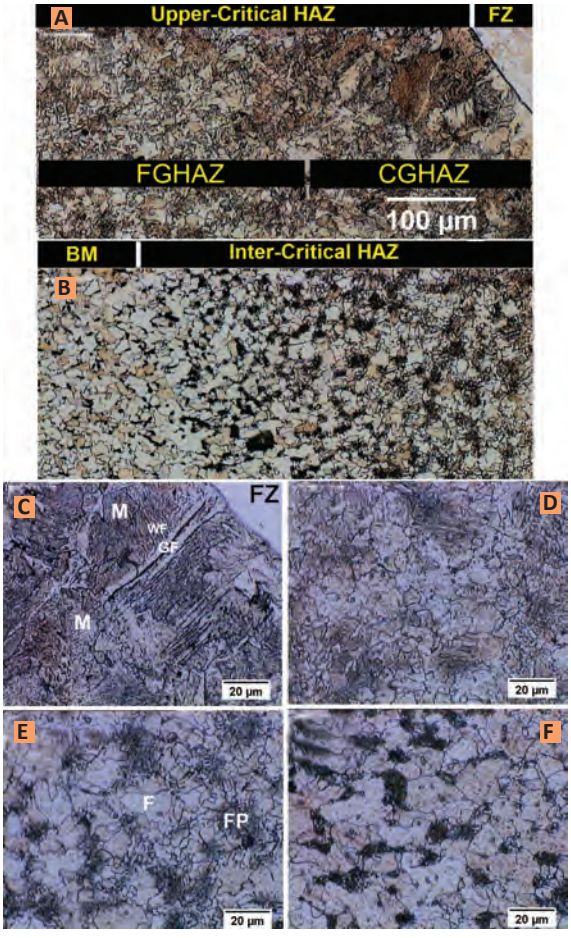

Fig. 4 — Microstructure gradient in the HAZ of low-carbon steels. A — Upper-critical HAZ, including CGHAZ and FGHAZ; B — inter-critical HAZ; C — detailed microstructure of CGHAZ; D–F — detailed microstructure of ICHAZ. The distance from fusion zone boundary is increased by moving from D to F. (M, F, WF, GF, and FP are martensite, ferrite, Widmanstätten ferrite, grain boundary ferrite, and fuzzy pearlite.)

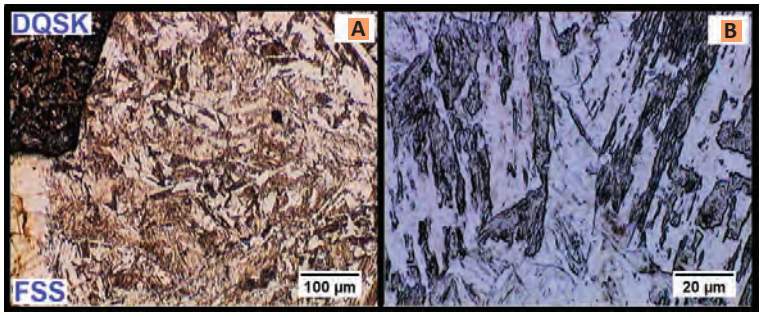

Fig. 5 — A and B — Fusion zone microstructure of FSS/DQSK dissimilar resistance spot weld.

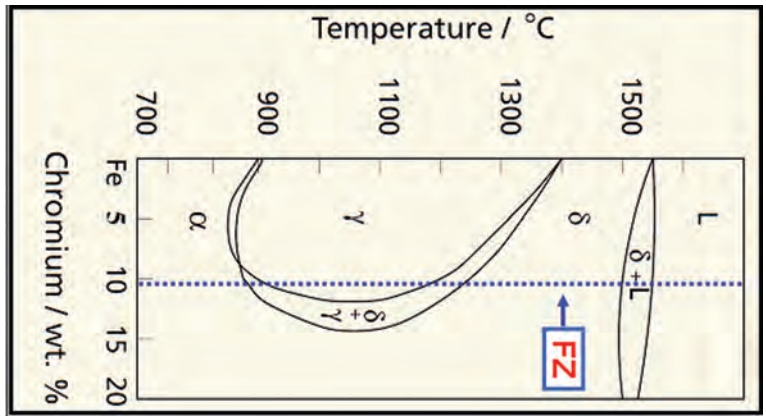

Fig. 6 — Fe-Cr phase diagram (Ref. 25). The chemical composition of the FZ is superimposed to the diagram.

tent of the alloys. Due to the low carbon content of the investigated AISI 430 steel (i.e., 0.024 wt-%), a very limited amount of austenite is formed in the LTHAZ. The high-temperature austenite is transformed to martensite during cooling. According to Fig. 3E, there is a small amount of martensite at the grain boundaries in the LTHAZ. Moreover, some reprecipitation of the carbides occurred.

HAZ of DQSK Steel

Figure 4A and B shows the microstructure gradient across the HAZ of the DQSK steel. The HAZ microstructure of the DQSK steel side is more heterogeneous than that of the FSS side due to martensitic and eutectoid transformations.

According to the temperature distribution, the HAZ of the DQSK steel side can be divided into two distinct metallurgical transformation zones, including upper-critical HAZ and inter-critical HAZ. The phase transformations in these zones are detailed as follows:

1) Upper-Critical HAZ (UCHAZ). This region experiences peak temperatures above A_{c3}, transforming BM microstructure into austenite. Depending on the peak temperature, the upper-critical HAZ can be divided into the following zones: coarse-grained HAZ (CGHAZ) and fine-grained HAZ (FGHAZ). The amount of grain growth in the HAZ is determined by the maximum temperature reached and the time it has been heated above the austenization temperature. In CGHAZ, which is adjacent to the FZ, both the high cooling rate and large austenite grain size coupled with the formation of the carbon-rich austenite promote the formation of the martensite (Ref. 1).

As can be seen, the microstructure CGHAZ consists of martensite, grain boundary ferrite, and Widmanstätten ferrite — Fig. 4C. Despite the very low carbon content DQSK steel (i.e., 0.04), the CGHAZ contains martensite. Martensite formation in the FZ is attributed to the high cooling rate of the RSW process due to the presence of water-cooled copper electrodes and their quenching effect as well as short welding cycle.

Gould et al. (Ref. 24) developed a simple analytical model predicting cooling rates of resistance spot welds. According to this model, the cooling rate for sheets having 1.5-mm thickness is about 4000 Ks^{-1}. For steels, the required critical cooling rate (Kh^{-1}) to achieve martensite phase in the microstructure can be estimated using the following equation (Ref. 25):

$$LogV = 7.42 - 3.13\,C - 0.71\,Mn - 0.37\,Ni - 0.34\,Cr - 0.45\,Mo \quad (1)$$

The calculated critical cooling rate for DQSK is 3684 Ks^{-1}. The experienced cooling rate in the FZ is higher

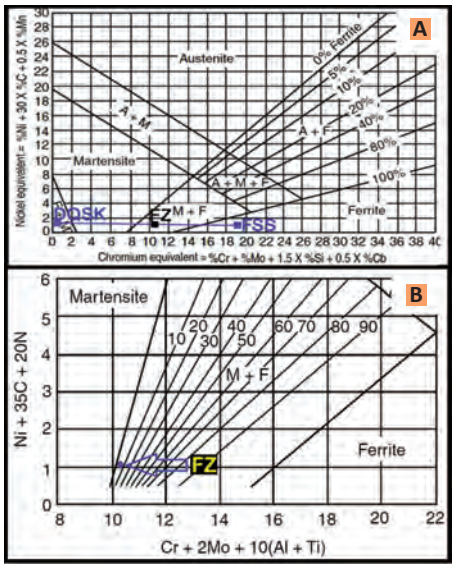

Fig. 7 — Prediction of FZ microstructure of dissimilar FSS/DQSK welds using the following: A — Schaeffler diagram; B — Balmforth and Lippold diagram.

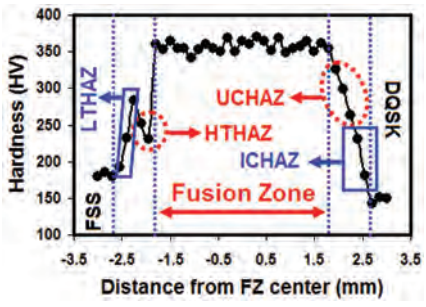

Fig. 8 — Typical hardness profile of dissimilar AISI 430/DQSK resistance spot welds.

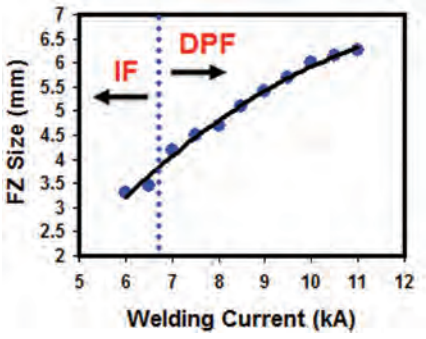

Fig. 9 — Effect of welding current on the FZ size and failure mode of dissimilar AISI 430/DQSK resistance spot welds.

than the critical cooling rate, so it is not surprising to find a martensite structure in the CGHAZ.

2) Inter-Critical HAZ (ICHAZ). In this region, the peak temperature is ranging between A_{c1} and A_{c3}, and the BM microstructure transforms into ferrite plus austenite during heating. Due to the fast welding cooling rates, austenite can transform subsequently into the martensite, bainite, or ferrite/pearlit depending on the cooling rate and hardenability of the steels. In the case of DQSK steel, due to low carbon content of the steel and hence its low hardenability, the microstructure consists of fine ferrite grains and pearlite, which pearlite amount decreases as it gets closer to BM — Fig. 4D, E. The volume fraction of pearlite in the ICHAZ is higher than that of in the BM due to reaustenization in the ICHAZ. Decreasing peak temperature in the intercritical region (i.e., by moving away the FZ line) results in lower pearlite volume fraction. As can be seen in Fig. 4, the ICHAZ is evidenced by fuzzy pearlite. The morphology of pearlite suggests that partial spheroidization of pearlite occurred in this region.

Fusion Zone

Figure 5A and B shows the microstructure of the FZ, indicating a dual-phase microstructure of martensite and ferrite phases. The volume fraction of ferrite and martensite is calculated as 28 and 72%, respectively. Phase transformations in the FZ are affected by the chemical composition and weld cooling rate. The FZ chemical composition of dissimilar combination can be estimated by considering the melting ratio of base metals. For FSS/DQSK welds, the melting ratio is considered as 60/40. Therefore, the FZ chemical composition of FSS/DQSK welds is Fe-10.2Cr-0.03C-0.038Mn-0.23Si-0.04Ni-0.01Mo.

Considering the low carbon content of the FZ, the Fe-Cr binary phase diagram (Ref. 26) can be used as a reference to track phase transformations in the FZ of the FSS/DQSK weld — Fig. 6. According to Fig. 6, the equilibrium phase transformation sequence is as follows:

Equilibrium Phase Transformation Sequence :

$$L \xrightarrow{I} L + \delta_{Ferrite} \xrightarrow{II} \delta_{Ferrite} \xrightarrow{III} \gamma_{Austenite} \xrightarrow{IV} \alpha_{Ferrite} \quad (2)$$

Under the nonequilibrium cooling condition, the formed austenite will be transformed to martensite.

Nonequilibrium Phase Transformation Sequence :

$$L \xrightarrow{I} L + \delta_{Ferrite} \xrightarrow{II} \delta_{Ferrite} \xrightarrow{III} \gamma_{Austenite} \xrightarrow{IV} \alpha'_{Martensite} \quad (3)$$

Regarding the transformation of austenite to martensite in the FZ, three points should be considered.

1) Austenite Stability. Self et al. (Ref. 27) in their work on the austenite stability and martensite formation in stainless steels, using a statistical regression analysis of the experimental data, obtained an expression for the martensite start temperature (M_s) as a function of alloy composition. Their equation is given as follows:

$$M_s = 526 - 12.5\,Cr - 17.4\,Ni - 29.7\,Mn - 31.7\,Si - 354\,C - 20.8\,Mo - 1.34\,(CrNi) + 22.41\,(Cr + Mo)C \quad (4)$$

where the chemical symbols indicate the weight percentage of the elements present.

According to Lippold and Kotecki (Ref. 28), this equation can be accurately used to examine austenite stability and estimate martensite start temperature for stainless steels. For FSS/DQSK welds, the M_s was calculated as 390°C, which is well higher than the room temperature. This indicates that the austenite is not stable at room temperature, and it transforms to martensite, as was observed.

2) Volume Fraction of Martensite. According to the binary Fe-Cr phase diagram (Fig. 6), a fully martensitic microstructure is predicted. However, according to metallographic examination, 28% ferrite is retained in the microstructure. The volume fraction of martensite in the FZ depends on the volume fraction of austenite present in the weld nugget at high temperatures, which is controlled by $\delta_{Ferrite} \rightarrow \gamma_{Austenite}$ phase transformation. This is a diffusion-controlled reaction. Upon a rapid cooling process (e. g., welding), the $\delta_{Ferrite} \rightarrow \gamma_{Austenite}$ transformation has less time to occur. Therefore, some amount of untransformed ferrite is retained in the

microstructure after stage III. Therefore, the phase transformation sequence in the FZ of dissimilar FSS/DQSK welds under rapid cooling of RSW can be considered as follows:

$$\begin{aligned} &\textit{Phase transformation sequences}\\ &\textit{under rapid cooling condition}\\ &L \xrightarrow{I} L+\delta_{Ferrite} \xrightarrow{II} \delta_{Ferrite}\\ &\xrightarrow{III} \gamma_{Austenite}+\delta_{Ferrite}\\ &\xrightarrow{IV} \alpha'_{Martensite}+\delta_{Ferrite} \end{aligned} \quad (5)$$

3) FZ Microstructure Prediction Using Conventional Constitution Diagrams. It has been proved that the conventional constitution diagrams (e. g., Schaeffler diagram and Balmforth and Lippold) can be used to predict the FZ microstructure of arc welds of joints involving stainless steels (Ref. 28). In this section, the ability of conventional constitution diagrams to predict weld FZ microstructure of dissimilar FSS/DQSK resistance spot welds is examined.

According to Fig. 7A, the predicted microstructure of a weld nugget using the Schaeffler diagram is the mixture of martensite and ferrite phases, as is observed in the FZ — Fig. 5A, B. Measurement using imageJ software showed that the volume fraction of ferrite phase in the FZ is about 28%. The Schaeffler diagram provides information about the present phases but not their quantities (Ref. 28). The Balmforth and Lippold diagram (Ref. 29) can be used for quantitative prediction of the relative amount of ferrite and martensite in the FZ.

In the case of the FSS/DQSK welds, the Balmforth diagram (Fig. 7B) predicts a martensitic microstructure with a small amount of ferrite (less than 5%), which is not in accordance with metallographic observations — Fig. 5B. As mentioned above, the amount of elevated austenite, which controls martensite volume fraction, depends on the $\delta_{Ferrite} \rightarrow \gamma_{Austenite}$ transformation. The higher cooling rate, the more δ-ferrite is retained in the microstructure. It has been shown that the cooling rate ranged from 2000 to more than 10,000 Ks^{-1} for sheet thickness ranging from 2 to 0.8 mm (Ref. 24).

Since the cooling rate in RSW is much higher than the arc welding, a higher volume fraction retained δ-ferrite is formed in the FZ of the weld made using RSW. Therefore, the presence of a high-volume fraction of δ-ferrite can be attributed to the rapid cooling rate of RSW, which suppresses the completion of post-solidification transformation of ferrite to austenite. Therefore, some corrections should be incorporated to the conventional constitution diagrams to accurately predict the microstructure of the FZ in resistance spot welded joints involving stainless steels.

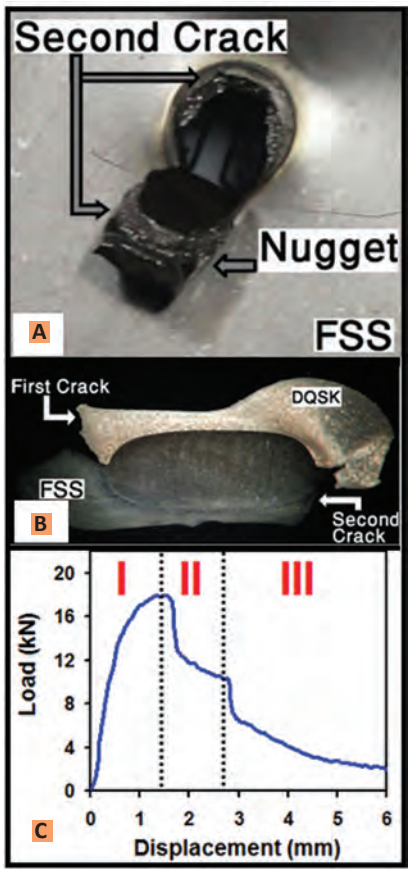

Fig. 10 — A — A typical DPF mode; B — macrographic of failure cross section; C — typical load-displacement curve showing a three-stage failure process. Stage I: work hardening and through thickness straining of both sheets. Stage II: severe necking and occurring the first crack in the DQSK steel. Stage III: second crack in the FSS side.

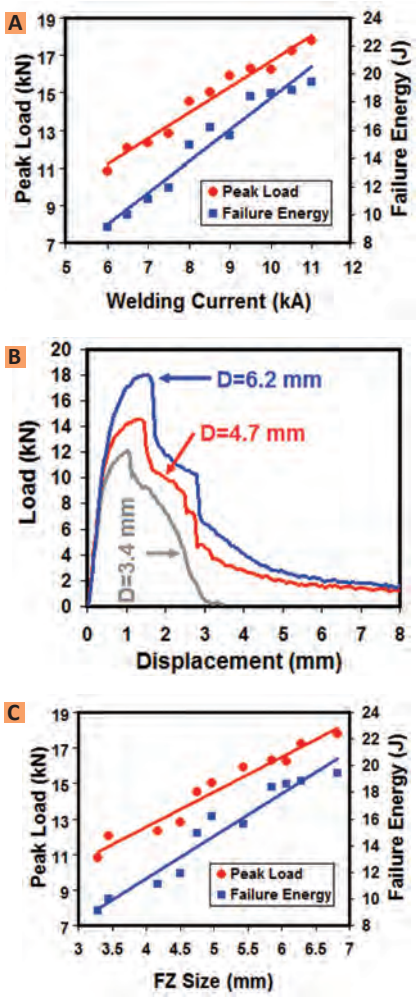

Fig. 11 — A — Effect of FZ size D on the load-displacement characteristics during the tensile-shear testing; B — welding current vs. peak load and energy absorption; C — fusion zone size vs. peak load and energy absorption of dissimilar AISI 430/DQSK resistance spot welds.

Hardness Characteristics

Hardness distribution across the resistance spot welds plays an important role in determining weld failure mode.

Figure 8 shows a typical hardness profile of FSS/DQSK welds. Hardness variation across the joint can be analyzed in terms of the microstructure evolution in the FZ and HAZs.

1) The hardness of the HAZ in the DQSK is higher than that of the base metal. The BM microstructure is essentially ferritic. The higher hardness of CGHAZ and ICHAZ compared to BM is due to the formation of martensite and pearlite in these regions, respectively.

2) The hardness of the HAZ in FSS is higher than that of the AISI 430 base metal. The higher hardness of the HTHAZ compared to the BM is due to the precipitation of carbides. The

higher hardness of the LTHAZ compared to the HTHAZ is due to martensite formation in ferrite grain boundaries and its finer grain size.

3) The hardness of the FZ is higher than both that of the base metals and HAZs, which can be attributed to the martensite formation in the FZ. The peak hardness in the HAZ of the DQSK is lower than the FZ hardness. The ferrite and martensite formed in the FZ are harder than those in the HAZ of DQSK. This can be related to the fact that ferrite and martensite phases in the FZ are enriched in chromium (Cr), an element that can strengthen both ferrite and martensite via a substitutional solid solution strengthening mechanism.

Failure Mode

Both interfacial failure (IF) and double pullout failure (DPF) modes were observed during the tensile-shear testing of the FSS/DQSK welds. It is well documented that the size of the FZ is the key physical weld attribute controlling the failure mode transition of spot welds (Refs. 10–17).

The effect of welding current on the FZ size is shown in Fig. 9, indicating the enlargement of the weld nugget by increasing welding current due to higher heat generation at sheet/sheet interface. According to Fig. 9, by increasing the welding current and FZ size, the failure mode was changed from IF to DPF. To avoid IF mode, a minimum welding current of 7 kA should be used for welding of the FSS/DQSK joint. The minimum FZ size required to avoid IF mode was 4.18 mm.

To analyze the failure mode transition of spot welds during the tensile-shear loading, Pouranvari and Marashi (Ref. 10) proposed a simple analytical model to predict the minimum FZ size (D_C) to ensure the pull-out failure mode as follows:

$$D_C = \frac{4t}{f}\left(\frac{H_{PFL}}{H_{FZ}}\right) \quad (6)$$

where t is the sheet thickness (mm), f is the ratio of shear strength to tensile strength of the FZ, and H_{FZ} along with H_{PFL} are hardness values (HV) of the FZ and PF location, respectively.

In this work, the model was used to evaluate the failure mode transition of the FSS/DQSK dissimilar joint.

- The hardness ratio of the FZ to PF location (i.e., DQSK's base metal) is about H_{FZ}/H_{PFL} = 350/140 = 2.5.
- There are no reported experimental data for the ratio of shear strength to tensile strength of the FZ, which is comprised of martensite and ferrite. Therefore, a theoretical value for the ratio of shear strength to tensile strength for the FZ is used. According to the von Mises criterion, the ratio of shear strength to tensile strength of metals is 0.58 (Ref. 30).
- Substituting the hardness ratio of 2.5 and the sheet thickness of 1.5 mm into Equation 4, a critical FZ size (D_C) of 4.1 mm is calculated.
- As can be seen in Fig. 8, in welding currents lower than 7 kA, the FZ size is lower than the D_C; consequently, the welds failed in IF mode. On the other hand, welds made at welding currents equal or higher than 7 kA exhibited higher FZ size than the D_C and hence failed in pullout mode.

As mentioned above, all spot welds made at a welding current higher than 6.5 kA failed at double pullout mode. No single pullout mode was observed.

Figure 10A shows the fracture surface of welds failed in pullout mode, indicating that the nugget is withdrawn from both sheets (i.e., double pullout mode). Figure 10B shows the metallographic cross section of a typical weld failed in DPF mode. Figure 10C is a representative load-displacement curve of the FSS/DQSK dissimilar weld. The pullout failure mechanism of spot welds in the tensile-shear loading is dominated by necking of the base metals. In the DPF, the nugget is completely torn off from the sheet, which experiences severe necking.

According to Fig. 10B and C, the PF of FSS/DQSK welds can be divided into the following stages:

Stage I. Both base metals are work hardened under loading and experienced through thickness straining.

Stage II. The failure is started by severe necking of one sheet. In this case, the PF location is determined by the competition between the necking of DQSK and FSS steel sheets. Since tensile strength and hardness of the DQSK is lower than that of the FSS sheet, DQSK sheet experiences a severe necking leading to the initiation of the failure at this point.

Stage III. After the welds experienced the first crack in the DQSK, the nugget is still connected to the other sheet. The final stage of the fracture occurs by partial separation of the nugget from the FSS sheet.

Mechanical Properties

To explore the quasistatic mechanical properties of the spot welds, peak load and energy absorption were measured. Figure 11A shows the effect of welding current on the peak load and energy absorption. The experimental results indicate that the welding current has a significant effect on the load carrying capacity and energy absorption capability of the spot welds under the tensile-shear static test. Load carrying capacity and energy absorption capability of spot welds depend on their physical attributes, especially weld nugget size, failure mode, and failure location strength.

According to Fig. 11B, the weld nugget size significantly affects the load-displacement characteristics of dissimilar FSS/DQSK welds. To examine the relationship between the peak load and failure energy and weld nugget size, a scatter plot of peak load (and failure energy) vs. weld size was constructed. Since the weld nugget has a asymmetrical shape, the FZ size at sheet/sheet interface in the DQSK steel, which is smaller than that of the FSS side, was measured.

As can be seen in Fig. 11C, there is a general linear relationship between the peak load (and also failure energy) and FZ size. Generally, increasing the FZ size increases the overall bond area and therefore increases the required force and energy for failure to occur.

Conclusions

Metallurgical and mechanical characteristics of dissimilar resistance spot welds between an AISI 430 ferritic stainless steel and DQSK low-carbon steel are investigated. The following conclusions can be drawn from this study:

1) Fusion zone is featured by dual-phase microstructure of ferrite and martensite. The transformation of

austenite to martensite can be explained by examination of austenite stability. The amount of martensite depends on austenite formation at high temperature as well as the extremely high cooling rate of RSW.

2) The main metallurgical features in the HAZ of FSS side are grain growth and carbide precipitation. The microstructure of the HAZ of the DQSK side is dictated by martensitic and eutectoid transformations.

3) Increasing the welding current led to the transition of failure mode from interfacial to double pullout mode. Failure mode transition is well explained considering the hardness distribution across the weldment. The DPF process can be divided into the following three stages: Stage I — work hardening and through thickness straining of both sheets, Stage II — severe necking and occurring the first crack in the DQSK steel, and Stage III — formation of the second crack in the FSS side. Accordingly, the mechanical response of the welds is controlled by the strength of the DQSK steel.

4) The FZ size at sheet/sheet interface in the DQSK side is the key macrostructural feature controlling the load bearing capacity and energy absorption capability of an AISI 430/DQSK dissimilar weld.

References

1. Pouranvari, M., and Marashi, S. P. H. 2013. Critical review of automotive steels spot welding: process, structure and properties. *Science Technology Welding Joining* 18: 361–403.

2. Pouranvari, M., and Marashi, S. P. H. 2010. Key factors influencing mechanical performance of dual phase steel resistance spot welds. *Science Technology Welding Joining* 15: 149–55.

3. Sun, X., Stephens, E. V., and Khaleel, M. A. 2008. Effects of fusion zone size and failure mode on peak load and energy absorption of advanced high-strength steel spot welds under lap shear loading conditions. *Engineering Failure Analaysis* 15: 356–67.

4. Radakovic, D. J., and Tumuluru, M. 2008. Predicting resistance spot weld failure modes in shear tension tests of advanced high-strength automotive steels. *Welding Journal* 87: 96-s to 105-s.

5. Pouranvari, M., Marashi, S. P. H., and Mousavizadeh, S. M. 2010. Failure mode transition and mechanical properties of similar and dissimilar resistance spot welds of DP600 and low carbon steels. *Science Technology Welding Joining* 15: 625–631.

6. Pouranvari, M. 2012. Susceptibility to interfacial failure mode in similar and dissimilar resistance spot welds of DP600 dual phase steel and low carbon steel during cross-tension and tensile-shear loading conditions. *Material Science Engineering A* 546: 129–138.

7. Yu, J., Choi, D., and Rhee, S. 2014. Improvement of weldability of 1 GPa grade twin-induced plasticity steel. *Welding Journal* 93(3): 78-s to 84-s.

8. Tumuluru, M. D. 2006. Resistance spot welding of coated high-strength dual-phase steels. *Welding Journal* 85(8): 31–37.

9. Pouranvari, M., and Marashi, S. P. H. 2010. Factors affecting mechanical properties of resistance spot welds. *Materials Science and Technology* 26: 1137–1144.

10. Pouranvari, M., and Marashi, S. P. H. 2011. Failure mode transition in AHSS resistance spot welds. Part I. Controlling factors. *Materials Science Engineering A* 528: 8337–43.

11. Pouranvari, M., Marashi, S. P. H., and Safanama, D. S. 2011. Failure mode transition in AHSS resistance spot welds. Part II: Experimental investigation and model validation. *Materials Science Engineering A* 528: 8344–52.

12. Pouranvari, M., Asgari, H. R., Mosavizadeh, S. M., Marashi, P. H., and Goodarzi, M. 2007. Effect of weld nugget size on overload failure mode of resistance spot welds. *Science Technology Welding Joining* 12: 217–25.

13. Safanama, D. S., Marashi, S. P. H., and Pouranvari, M. 2012. Similar and dissimilar resistance spot welding of martensitic advanced high-strength steel and low carbon steel: metallurgical characteristics and failure mode transition. *Science Technology Welding Joining* 17: 288–94.

14. Pouranvari, M., and Marashi, S. P. H. 2012. Failure mode transition in AISI 304 resistance spot welds. *Welding Journal* 91: 303-s to 309-s.

15. Sun, X., Stephens, E. V., and Khaleel, M. A. 2007. Effects of fusion zone size and failure mode on peak load and energy absorption of advanced high-strength steel spot welds. *Welding Journal* 86(1): 18-s to 25-s.

16. Hernandez, V. H. B., Kuntz, M. L., Khan, M. I., and Zhou, Y. 2008. Influence of microstructure and weld size on the mechanical behaviour of dissimilar AHSS resistance spot welds. *Science Technology Welding Joining* 13: 769–776.

17. Marya, M., and Gayden, X. Q. 2005. Development of requirements for resistance spot welding dual-phase (DP600) steels Part 1 — The causes of interfacial fracture. *Welding Journal* 84(11): 172-s to 182-s.

18. Marashi, P., Pouranvari, M., Amirabdollahian, S., Abedi, A., and Goodarzi, M. 2008. Microstructure and failure behavior of dissimilar resistance spot welds between low carbon galvanized and austenitic stainless steels. *Materials Science and Engineering A* 480: 175–80.

19. Alenius, M., Pohjanne, P., Somervuori, M., and Hanninen, H. 2006. Exploring the mechanical properties of spot welded dissimilar joints for stainless and galvanized steels. *Welding Journal* 85: 305-s to 313-s.

20. Pouranvari, M., and Marashi, S. P. H. 2009. Similar and dissimilar RSW of low carbon and austenitic stainless steels: Effect of weld microstructure and hardness profile on failure mode. *Materials Science Technology* 25: 1411–6.

21. Recommended practices for test methods for evaluating the resistance spot welding behavior of automotive sheet steel materials. ANSI/AWS/SAE/D89-97. Miami, Fla.: AWS; 1997.

22. Kou, S. 2003. *Welding Metallurgy*. Hoboken, N.J.: John Wiley & Sons, Inc.

23. Alizadeh-Sh, M., Marashi, S. P. H., and Pouranvari, M. 2014. Resistance spot welding of AISI 430 ferritic stainless steel: Phase transformations and mechanical properties. *Materials and Design* 56: 258–63.

24. Gould, J. E., Khurana, S. P., and Li, T. 2006. Predictions of microstructures when welding automotive advanced high-strength steels. *Welding Journal* 85(5): 111-s to 116-s.

25. Easterling, K. E. 1993. Modelling the weld thermal cycle and transformation behavior in the heat-affected zone. *Mathematical Modelling of Weld Phenomena*. Eds. H. Cerjak and K. E. Easterling. The Institute of Materials.

26. Carrouge, D., Bhadeshia, H. K. D. H., and Woollin, P. 2002. Microstructural change in high-temperature heat-affected zone of low-carbon weldable 13% Cr martensitic stainless steels. *Proc. Stainless Steel World Conference*, Houston, Tex., pp. 61–67.

27. Self, J. A., Olson, D. L., and Edwards, G. R. 1987. The stability of austenitic weld metal. *NBS Publication on Cryogenic Properties of Metals*: 181–189.

28. Lippold, J. C., and Kotecki, D. J. 2005. *Welding Metallurgy and Weldability of Stainless Steels*. New Jersey: John Wiley & Sons.

29. Balmforth, M. C., and Lippold, J. C. 2000. A new ferritic-martensitic stainless steel constitution diagram. *Welding Journal* 79(12): 339-s to 345-s.

30. Hertzberg, R. W. 1996. *Deformation and Fracture Mechanics of Engineering Materials*, 2nd ed. John Wiley & Sons.